

Influence of indium doping on the morphology of ZnS nanostructures grown by a vapor–solid method

Cite this: *CrystEngComm*, 2013, 15, 7080

Belén Sotillo,* Yanicet Ortega, Paloma Fernández and Javier Piqueras

Pure and In-doped ZnS structures have been grown using a VS method. Thermal treatments have been performed at temperatures ranging from 1000 to 1200 °C, during 15 to 17 hours in a N₂ overpressure environment. Nanowires and nanoribbons are the main kind of structures obtained for pure ZnS, depending on the deposition temperature. In the case of ZnS:In, nano- and microstructures, nanoribbons, hierarchical structures and nanoplates are obtained, depending on the In content in the starting material and on the deposition temperature. Nanoplates are the dominant structures for the higher In content. The influence of the impurity incorporation on the morphology of the structures has been studied by transmission electron microscopy. While in pure ZnS wires and ribbons two main growth directions are observed ([0001] and [10 $\bar{1}$ 0]), indium doped structures show a greater variety of morphologies associated with different growth behavior.

Received 24th May 2013,
Accepted 3rd July 2013

DOI: 10.1039/c3ce40920a

www.rsc.org/crystengcomm

Introduction

II–VI semiconductors have properties of interest, such as a large direct band gap, chemical stability and a large exciton binding energy, which make them excellent candidates for nano-optoelectronic applications.¹ In particular, ZnS has the largest bandgap among II–VI semiconductors, with a value that slightly depends on the crystal structure. The cubic (zinc-blende) phase is the most stable at room temperature, with a gap of about 3.72 eV, whereas the hexagonal (wurtzite) phase is more stable above 1200 °C and has a gap of 3.77 eV.² For ZnS nanostructures, a phase transition could occur at lower temperatures, which permits the stabilization of the wurtzite phase at a lower temperature^{3,4} and hence, the two polytypes could coexist.^{5,6}

As usual in semiconductors, doping of ZnS allows us to change some of its properties, like conductivity or luminescence. Elements from III-group (Al, Ga, In) can increase the low conductivity of ZnS⁷ and have been traditionally used as coactivators with Au, Ag or Cu to improve its luminescent properties.⁸ In a previous work,⁹ we have reported the influence of indium incorporation on the luminescence of ZnS nanostructures grown by evaporation routes (Vapor–solid, VS). In the present work, a more detailed study of the growth process and of the morphology and structural features of the In doped nanostructures is accomplished. Indium incorporates in the Zn positions of the ZnS lattice. As In has a larger radius than Zn, the doping process induces strain in the lattice

that can change the surface energy as well as the preferential growth direction of the nanostructures. This effect, which has been observed in other doped systems, like ZnO:In¹⁰ and ZnO:Sn,¹¹ could be used to control the morphology of the ZnS nanostructures in order to make them suitable for specific applications, such as UV sensors,¹² gas sensors,^{13,14} photocatalysis¹⁵ or field-emission devices.¹⁶ ZnS low dimensional structures have been grown by several methods. In particular, evaporation processes have been successfully used to grow thin films¹⁷ as well as nanostructures.^{18–20} Contrary to the case of ZnO, the effect of In incorporation during the thermal growth of ZnS nano- or microstructures has been scarcely investigated. In this work, In doped elongated micro- and nanostructures with different In contents have been grown by a VS method and, in addition to nanoribbons, nanoplates and hierarchical structures, other not previously reported ZnS structures with a sword-like shape were synthesized. The mechanisms leading to the formation of structures with different morphologies have been investigated by scanning electron microscopy (SEM), energy dispersive spectroscopy (EDS), electron backscatter diffraction (EBSD), transmission electron microscopy (TEM) and Raman spectroscopy.

Experimental section

The starting material used to grow pure nanostructures was 99.99% commercially available ZnS powder. For obtaining In doped structures, a mixture of ZnS and In₂S₃ (99.99%) powders was used. The amount of In₂S₃ in the mixture was 5, 10 and 15 wt% which corresponds to 1.51, 3.07, 4.66 at% of In, respectively. The mixture was homogenized using a centrifugal

Departamento de Física de Materiales, Facultad de Ciencias Físicas, Universidad Complutense de Madrid, 28040 Madrid, Spain. E-mail: bsotillo@ucm.es; Fax: +34 91 394 4547; Tel: +34 91 394 4865

ball mill during 5 h. The powder was compacted under a compressive load to form disk-shaped pellets. The dimensions of the pellets were about 7 mm in diameter and a thickness of 2 mm.

Thermal treatments have been performed in a N_2 atmosphere. The furnace chamber was first evacuated to 10^{-2} Torr and then the gas was introduced at a constant rate to maintain a pressure of about 700 Torr. The treatment was performed in two steps, one at 1000 °C during 15 hours, followed by a second step at 1200 °C for two additional hours. This procedure has proved to be the best option: nuclei formed during the first step act as additional nucleation sites in the second step, favouring the growth of a large amount of nanostructures. The source pellet was placed in the hot region of the furnace so that evaporation is quite efficient and the structures, undoped or In doped depending on the precursor used, grow at different points of the furnace alumina tube (*i.e.* at different deposition temperatures). As described below, the morphology of the structures depends strongly on the deposition temperature, which is between 500 and 900 °C (for simplicity, we will refer to the temperature range in the first step of the thermal treatment).

X-ray diffraction analysis (XRD) of the starting material and of the treated samples has been done by means of a Philips X'Pert PRO diffractometer. SEM measurements have been performed either in a FEI Inspect or a LEICA 440 Stereoscan. EDS measurements have been done with a Bruker AXS Quantax system attached to the LEICA SEM. Raman measurements have been carried out in a Horiba Jobin Yvon LABRAM-HR Raman spectrometer using the 325 nm line from a He–Cd laser at room temperature. Laser light has a linear polarization. TEM measurements have been done in a JEOL JEM-2100HT. Electron backscatter diffraction (EBSD) measurements have been carried out on a Bruker e-Flash EBSD Detector attached to an FEI SEM.

Results and discussion

As previously reported,²¹ the structures obtained in the case of pure ZnS are nanowires, nanoribbons and microrods. The specific morphology depends on the deposition temperature: nanowires grow mainly in the region of the furnace tube at about 500 °C while ribbons and rods grow at deposition temperatures near 900 °C (Fig. 1). The diameter and the width of the nanowires and the nanoribbons are under 100 nm, with lengths in both cases of tens of micrometers. Rods usually present diameters of micrometers and lengths of hundreds of micrometers.

In the case of In doped ZnS, the obtained structures show a predominance of two-dimensional morphologies, such as ribbons, nanoplates and swords, and hierarchical growth is also present. In incorporation appears to retard a directional growth and to favor transverse growth. Similar influences of doping on the morphology of ZnO micro- and nanostructures grown by thermal methods have been reported for Sn,¹¹ In,¹⁰

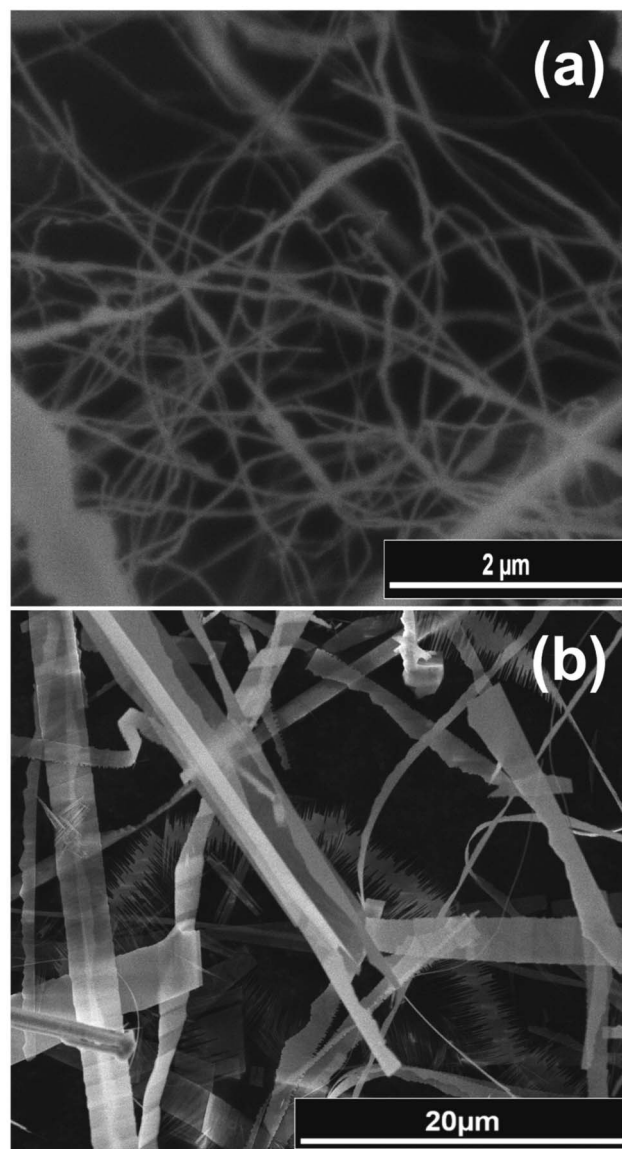


Fig. 1 SEM images of the typical pure ZnS nanostructures obtained: (a) nanowires, (b) different types of nanoribbons.

and Al^{22,23} doping. The influence on the growth direction and hence on the morphology is attributed to the strain induced by the size difference between the dopant ion and the Zn ion of the host. We suggest that this effect contributes to the 2D growth of the In doped ZnS structures of this work. On the other hand, hierarchical growth has also been observed in many doped ZnO systems and it has been attributed to an autocatalytic effect associated with the metallic dopant ion.²⁴ Segregation of In would cause the formation of a liquid drop which would act as catalyser in a similar way to a vapour–liquid–solid (VLS) process.

The shape of the In doped ZnS structures has been found to depend on the deposition temperature. In particular, two deposition temperature ranges are observed, the first one between 500 and 800 °C, and the second one between 850 and

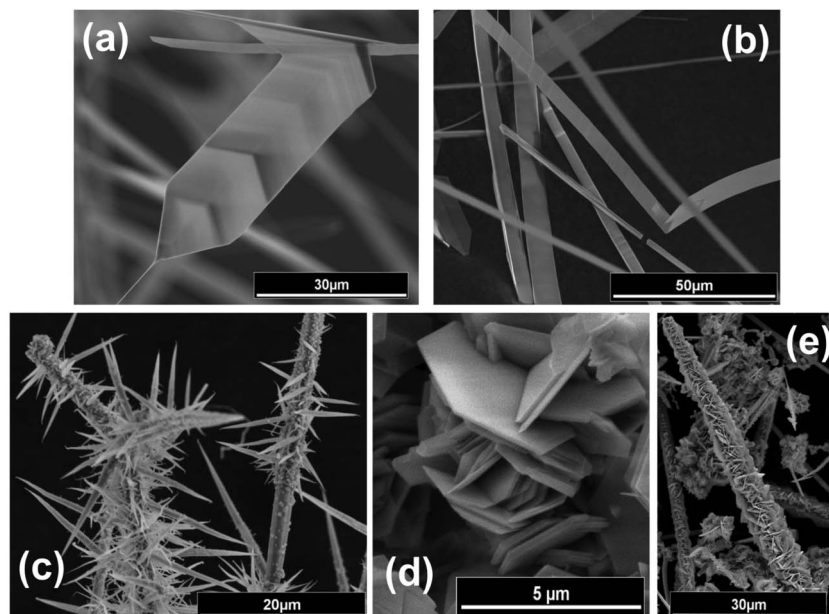


Fig. 2 SEM images of the different morphologies of the ZnS:In structures, depending on the deposition temperature and the In content in the starting material. (a) and (b) Temperature range between 850 and 900 °C. (c)–(e) Temperature range between 500 and 800 °C. (a) Sword. (b) Ribbons. (c) Hierarchical structures for an initial In content of 1.51 at%. (d) Nanoplates obtained for an initial In content of 3.07 and 4.66 at%. (e) Hierarchical structure with nanoplates for an initial In content of 3.07 at%.

900 °C. For the higher temperature range, pointed plate-shaped structures, hereinafter designated as swords (Fig. 2a) and ribbons (Fig. 2b), are obtained, no matter the In content in the starting material (1.51, 3.07, 4.66 at% of In). The thicknesses of the ribbons and swords range from hundreds of nanometers to several micrometers. The widths are of tens of micrometers and their lengths range from a few micrometers to hundreds of micrometers. For the lower temperature range and an initial In content of 1.51%, hierarchical structures consisting of nanoneedles growing from a central stem are formed (Fig. 2c). By increasing the initial In content (3.07, 4.66 at% of In), intercrossed hexagonal nanoplates, similar to those observed in ZnO:In,¹⁰ or ZnO:Sn,¹¹ with typical thicknesses between 100 and 200 nm are obtained (Fig. 2d). Fig. 2e shows the evolution from nanoneedles to nanoplates when the In content increases.

XRD measurements show that the starting ZnS powders are of a zinc-blende phase (JCPDS card No. 05-0566). In the as-grown pure ZnS structures, the hexagonal wurtzite phase (JCPDS card no. 36-1450) is also detected. At high deposition temperatures, the reflections associated with the wurtzite structure become dominant but small peaks corresponding to the cubic phase remain (Fig. 3a). In the case of the doped structures, all the reflections can be assigned to the wurtzite phase of ZnS (Fig. 3b).

EDX measurements in SEM performed on the different growth products reveal a homogeneous distribution of all the elements, with a slightly S poor stoichiometry, and confirm the presence of indium in the doped structures. The amount of indium incorporation, which is homogeneous within each

structure, seems to depend on the deposition temperature. EDX measurements in the hierarchical structures obtained at lower temperature regions show an In content between 0.2 and 1 at%, while in the nanoplates, the In content is slightly higher (0.4–1.5 at%). The degree of In incorporation in the nanoplates does not vary significantly when the at% of In in the starting material increases. For the swords and ribbons, although a weak In peak is observed, its intensity is below the limit to give a reliable quantification. We have also reported a change in

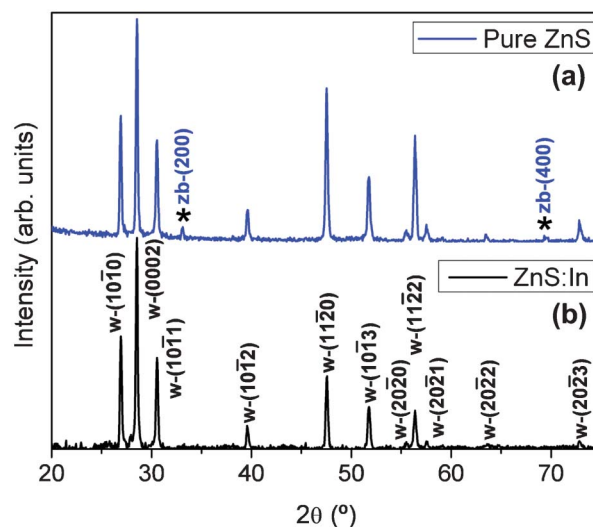


Fig. 3 Typical XRD patterns for (a) pure ZnS; (b) In doped ZnS (zb stands for zinc-blende and w for wurtzite).

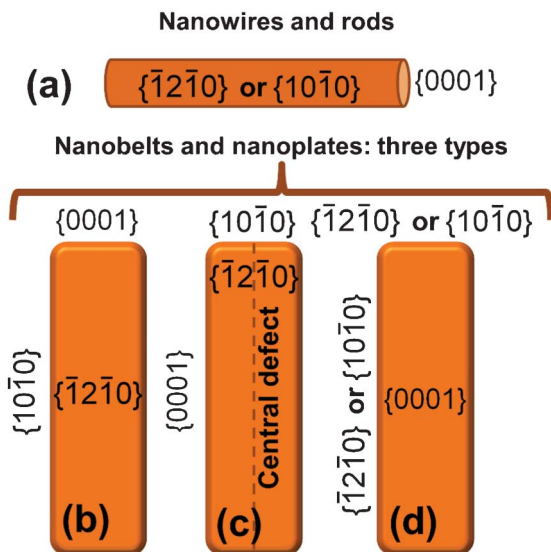


Fig. 4 Different types of nanostructure morphologies that can be obtained in wurtzite structure materials, depending on the growth directions.

the cathodoluminescence of all the doped structures compared to the pure structures luminescence.⁹

It is known that micro- and nanostructures of materials with a wurtzite structure grown by a vapor solid process show three different types of fast growth directions, $\langle\bar{1}2\bar{1}0\rangle$, $\langle10\bar{1}0\rangle$ and $\pm[0001]$.²⁵ In the case of nanowires or rods, the growth occurs along the $\pm[0001]$ direction (Fig. 4a), while in nanobelts, three different types of growth can be found, as illustrated in Fig. 4b–d and discussed in ref. 25. It is to be noticed that the $\{0001\}$ surfaces are polar so that opposite faces in the crystal correspond to positively charged Zn $\{0001\}$ and negatively charged S $\{000\bar{1}\}$ faces, respectively, in the particular case of ZnS. Polar faces normally have different growth rates, with a higher rate on the positive face, and their growth is irregular with the formation of facets. For this reason, the nanobelts with the morphology shown in Fig. 4c would not show smooth lateral faces. This effect is observed by TEM analysis performed on pure nanostructures, as shown in Fig. 5. In part (a) of this figure, a nanobelt with smooth sides is observed. This kind of morphology would correspond to growth along the $\pm[0001]$ direction, the upper surface being $\{\bar{1}2\bar{1}0\}$ and lateral $\{10\bar{1}0\}$ faces and hence, smooth non polar surfaces.²⁶ These growth directions are confirmed with the FFT made on a free defect area of the nanobelt. A different type of belt is shown in part (b) of Fig. 5. In this case, as can be obtained from the SAED pattern, the growth takes place along $[10\bar{1}0]$, the lateral faces being $\{0001\}$ type, either Zn- (positive polarity) or S-terminated (negative polarity). The presence of saw-like ribbons is due to the faceted growth on the positive polar Zn face, as shown in Fig. 4b, where teeth appear in the Zn-surface and a smooth edge in the S-surface.²⁷ Also, ribbons with teeth on both sides have been observed (Fig. 5c). This kind of ribbon grows like the saw-like ribbons, according to TEM measurements, and the differences in the chemical

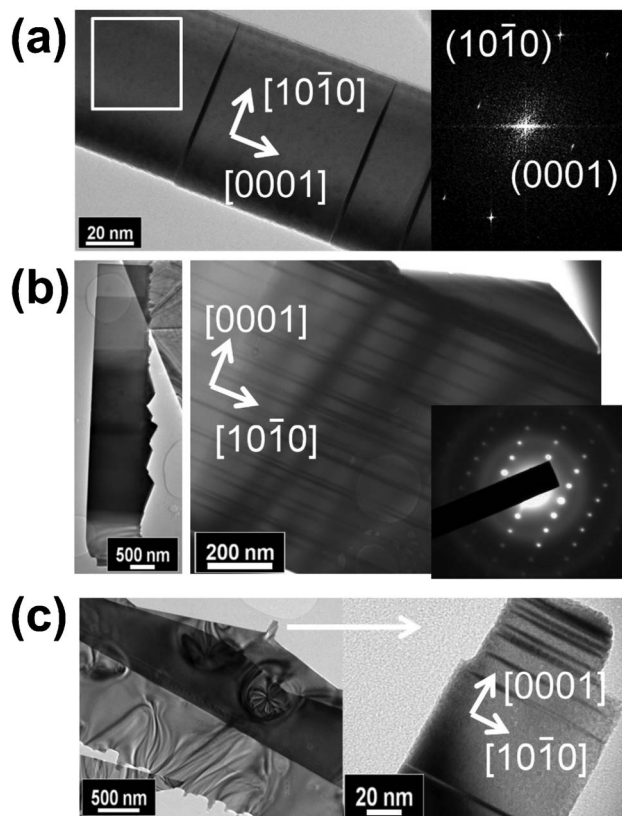


Fig. 5 TEM images of the three ribbon morphologies observed in our samples: (a) a nanobelt with smooth sides with its FFT made on an area free of defects (marked with a white square); (b) a saw-like nanoribbon, with a magnified image of a region where the diffraction pattern has been taken; (c) a nanoribbon with teeth on both sides, with a magnified image of one tooth.

activity of the Zn and S terminated surfaces is revealed by the number of teeth that appear on each side and in the presence of the saw on only one side, as Fig. 5c shows. The other feature observed in the TEM images of Fig. 5 is a high density of stacking faults, perpendicular to the $[0001]$ direction. These faults would be associated with a change in the stacking sequence of the wurtzite structure (ABAB...) to the zinc-blende structure (ABCABC...), which is energetically favorable as the zinc-blende phase is more stable at room temperature.

TEM measurements have also been performed on the doped structures. For the nanoplates (Fig. 6a and b) obtained at lower deposition temperatures and higher In contents, a change in the growth behavior is observed. As can be seen in the diffraction pattern (Fig. 6c) and in the FFT (Fig. 6d), the growth along the $[0001]$ direction seems to be inhibited by the presence of In and the nanoplates grow symmetrically along the directions of the $\langle10\bar{1}0\rangle$ family, adopting a well defined hexagonal shape (Fig. 6b). As expected, since practically no growth occurs along the $[0001]$ direction, no stacking faults are observed in the nanoplates. A similar growth direction has been observed in sheets of ZnS:Ga.²⁸ In many cases, nanoplates are surrounded by small crystallites with a much higher In content (around 3.5% at., according to the EDX

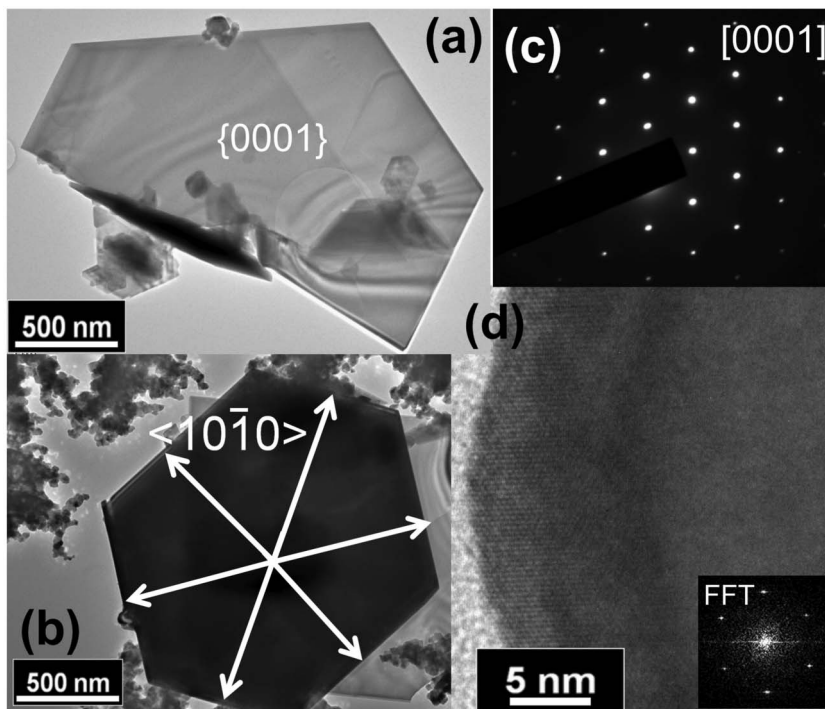


Fig. 6 (a) and (b) TEM images of different nanoplates. (a) shows a half-plate and (b) a complete hexagonal plate. (c) Typical SAED pattern recorded from hexagonal nanoplates. (d) High-resolution TEM image of one vertex of a nanoplate, with its FFT.

measurements in the TEM) and then it seems they accumulate all the In that cannot be incorporated into the plates. XRD reveals the total absence of In_2S_3 or In_2O_3 and it can then be assumed that the In has been incorporated into the ZnS lattice, most likely as In^{3+} .²⁹ A similar effect has been reported in ZnS:Eu, where a defect complex is formed to compensate for the charge defect.³⁰

The thermal growth of ZnS ribbons has been widely reported,^{19,31,32} however, the influence of In on the growth process and, in particular, the growth of the so-called swords, has not yet been described. As we have seen in the nanoplates, In favors growth along the $\langle 10\bar{1}0 \rangle$ directions. A similar effect has been reported in other In doped systems.¹⁰ In the case of the less doped nanostructures, two main effects on the microstructure have been observed upon In doping: the reduction of the density of planar defects and the appearance of swords instead of ribbons. Although ribbons and swords are both bidimensional structures, the growth direction is different. For In doped material, only ribbons with smooth sides are observed (Fig. 7a). Stacking faults appear perpendicular to the [0001] growth direction but with a lower density than in undoped ribbons. As described above, XRD show weak peaks for the cubic phase only in undoped samples. This suggests that indium incorporation favors the growth of a single hexagonal phase and hence, the stacking faults are less abundant in doped samples. In fact, saw-like ribbons (in which the density of planar defects is higher) are not obtained when In incorporates into the structures. Nanoswords can be considered to be formed by two blades, separated by a central

defect parallel to the growth direction and extending all along the sword, from the base (Fig. 7b) to the tip (Fig. 7c). From the SAED pattern of one blade, we can identify the diffractions associated with the (0001), (10 $\bar{1}0$) and (10 $\bar{1}1$) planes (Fig. 7d). Similar to pure ZnS, the [0001] direction is parallel to the long axis of the doped ribbons, whereas in the so-called swords, neither the [0001] nor [10 $\bar{1}0$] directions are parallel to its long axis. Each blade grows along a direction that is a combination of the [0001] and [10 $\bar{1}0$] directions. The sword axis forms an angle of 60° with the [0001] direction and a 30° angle with the [10 $\bar{1}0$] direction of each blade, which corresponds to the [10 $\bar{1}1$] direction (Fig. 7b). The stacking faults that usually appear in {0001} planes are also observed in both blades, forming an angle of 30° with the central defect (Fig. 7b). From this, we can also deduce that the planes at the tip of the sword belong to the {0001} family (Fig. 7c). As the [0001] direction of each blade forms a 60° angle with the central defect and that this defect could be a twin that separates two crystals with different orientations (Fig. 7e). Similar defects have been observed in other ZnS nanostructures and have been associated with twins in the [1013] plane,^{33,34} which is the lowest energy twin boundary in wurtzite crystals, according to Béré *et al.*³⁵

The relative orientation of the two blades has been determined by EBSD analysis performed on both blades of a sword. The same pattern is recorded at different points of a blade. An example of the typical Kikuchi patterns obtained on a pair of blades is presented in Fig. 8. For the sake of simplicity, we have marked the lines associated with the {0001} planes and with the {10 $\bar{1}0$ } planes. Also, the pole figure

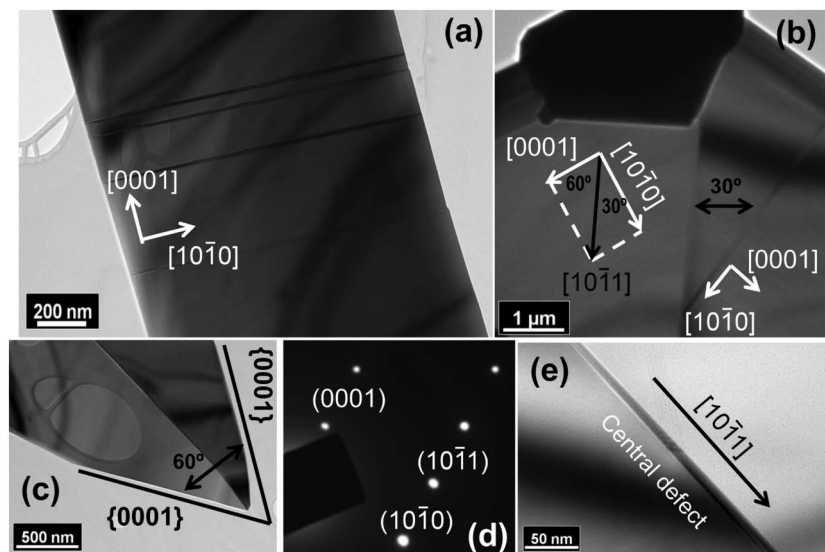


Fig. 7 (a) TEM image of a ZnS:In ribbon. (b) The base of a sword, where the nucleation point can be seen. The angle between the central defect and a defect in the right blade is marked. The crystallographic directions are indicated on both blades. (c) The tip of the sword. (d) Typical SAED pattern recorded from one blade. (e) Magnified image of the central defect.

associated to each Kikuchi pattern is drawn using the software of the EBSD detector. The pole figures are obtained in the zone axis of the blades, in both cases $\langle 1\bar{2}10 \rangle$. Comparing both Kikuchi patterns, we can see that the $\{0001\}$ planes in one of the blades are rotated about 60° with respect to the other (or the $[0001]$ direction, parallel to the line of the $(10\bar{1}0)$ planes of

one blade, is rotated 120° with respect to the other). This agrees with the TEM analysis.

From the SE images and the TEM and EBSD analysis, we propose the model for the growth of the swords, presented in Fig. 9. The nucleation can start either on the substrate where the structures are obtained (alumina) or on another structure. The growth starts in a nucleation point (Fig. 9, step 1). Then,

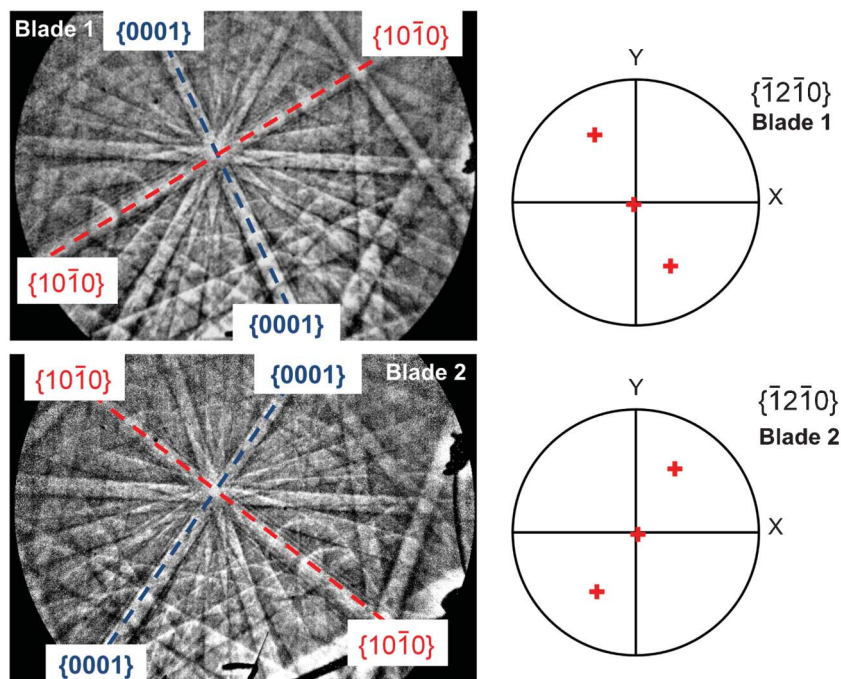


Fig. 8 EBSD patterns recorded on two blades of the same sword, without changing its orientation with respect to the EBSD detector. The pole figures, obtained in the $\langle 1\bar{2}10 \rangle$ zone axis, are presented on the side of both patterns. XY represents the plane where the structure is.

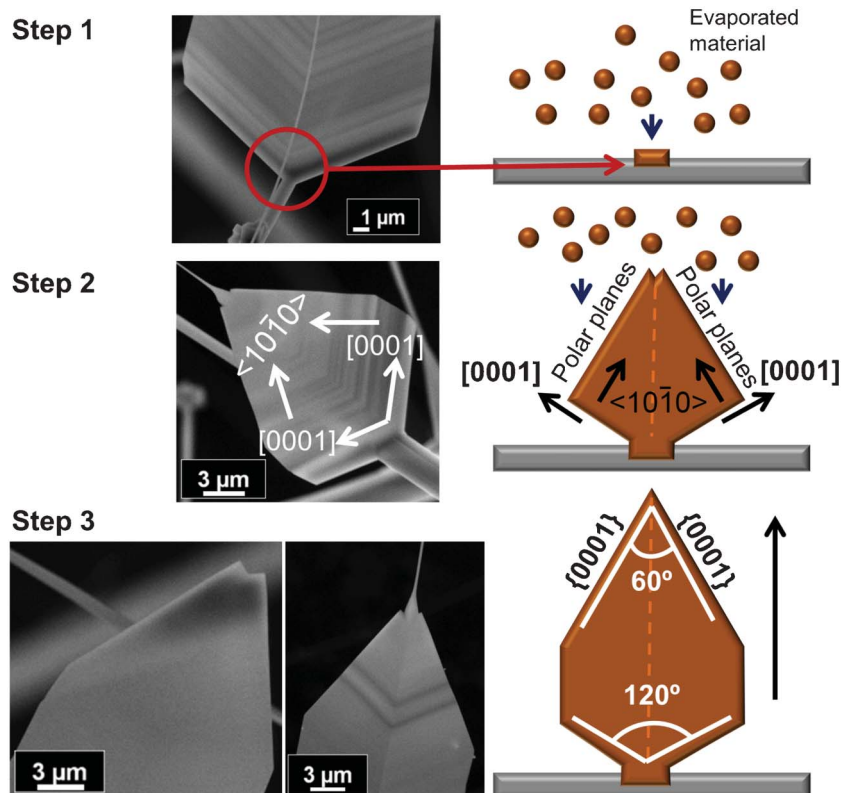


Fig. 9 Growth model of the ZnS:In swords. Step 1: formation of a nucleation site where the evaporated material can deposit to start the growth. Step 2: the sword begins to grow along the two fastest directions in ZnS: [0001] and $[10\bar{1}0]$. Step 3: the faster growth along $[10\bar{1}0]$ makes the sword an elongated structure.

the sword begins to grow along the two fastest directions in ZnS: [0001] and $[10\bar{1}0]$. (Fig. 9, step 2). The central defect accommodates the 120° disorientation between the two blades. Then, the sword continues to grow in both directions, but faster in the $[10\bar{1}0]$ direction (as we have seen in the nanoplates, indium favors growth along the $[10\bar{1}0]$ direction), making the sword an elongated structure (Fig. 9, step 3). The tip is formed by planes at 60° , corresponding to the $\{0001\}$ family. The presence on the tip of several swords of other structures, like nanowires or rods, indicates the catalytic

activity of the planes on the tip. The plane that forms the largest surfaces of the swords is the non polar $\{1\bar{2}10\}$ plane. In fact, this could be considered a variety of the second types of ribbons shown in Fig. 4, where the upper surface of the ribbon is $(1\bar{2}10)$, but the [0001] and $[10\bar{1}0]$ form an angle with the longitudinal axis of the structure and a planar defect appears in the centre of it.

The different crystal orientation of the two blades in the sword also affects the Resonant Raman spectra. In Fig. 10, the Resonant Raman spectra obtained from both blades are

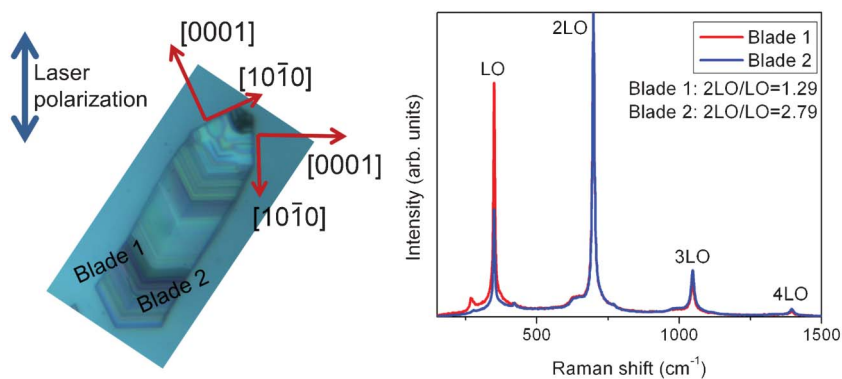


Fig. 10 Resonant Raman spectra recorded on each blade of a sword. The 2LO/LO ratio of each spectrum is also presented. The growth directions of the sword are indicated on the optical micrograph.

shown. The spectra show peaks at 350 cm^{-1} , 699 cm^{-1} , 1047 cm^{-1} and 1395 cm^{-1} and are similar to the spectra from bulk ZnS.³⁶ These peaks are associated with optical longitudinal phonons (LO) and their replicas. A change in the relative intensity between the LO peak and 2LO peak is observed when we compare the spectra from each blade, maintaining an unchanged laser polarization during the experiment. It has been observed that the blade which has its $[10\bar{1}0]$ direction closer to the laser polarization has a higher 2LO/LO ratio, as shown in Fig. 10. This effect could arise from differences in the light absorption associated with different crystal orientations. However, further studies are required to clarify this point. Another effect observed in swords and in ribbons is the change of the 2LO/LO ratio when the complete structure is rotated with respect to the laser polarization. When the laser polarization is parallel to the long axis of the structure, the intensity of the Raman spectrum and the 2LO/LO ratio is at its maximum, while when the laser polarization is perpendicular to the long axis, the intensity of the Raman spectrum and the 2LO/LO ratio is at its minimum. This shape effect has been previously described for CdS nanowires and is associated with a reduction of the local internal field inside the structure when the incident field is perpendicular to the wire axis.³⁷

Conclusions

Micro- and nanostructures of pure and indium doped ZnS have been synthesized by a vapor–solid method. The pure structures are mainly nanowires and nanoribbons with $[0001]$ or $[10\bar{1}0]$ growth directions. These two directions produce two kinds of ribbons, the first with smooth sides and the second with a saw on one side. Stacking faults associated with the $\{0001\}$ planes are observed in all the structures. Nanoplates, hierarchical structures and swords are the main structures of ZnS:In. Hierarchical growth is attributed to a catalytic effect associated with the dopant ion. Hexagonal nanoplates, which are the structures with the higher In content, grow along the $\langle 10\bar{1}0 \rangle$ directions. In the case of the swords, with lower In incorporation, slight changes are observed. Swords are formed by two crystals growing along the $[10\bar{1}1]$ direction and separated by a twin. The change in the growth direction in the nanoplates and swords is attributed to the strain induced by the size difference between the In ion and the Zn ion of the host. Further measurements are needed to determine the nature of the dopant sites and its influence on the growth kinetics.

Acknowledgements

This work has been supported by MINECO (Projects MAT 2012-31959 and CSD2009-00013). B. Sotillo acknowledges the Ministerio de Educación (Subprograma FPU) of Spain for financial support.

References

- J. Jie, W. Zhanga, I. Bello, C.-S. Lee and S.-T. Lee, *Nano Today*, 2010, **5**, 313–336.
- X. Fang, T. Zhai, U. K. Gautam, L. Li, L. Wu, Y. Bando and D. Golberg, *Prog. Mater. Sci.*, 2011, **56**, 175–287.
- S. B. Qadri, E. F. Skelton, D. Hsu, A. D. Dinsmore, J. Yang, H. F. Gary and B. R. Ratna, *Phys. Rev. B: Condens. Matter*, 1999, **60**, 9191–9193.
- S. Li, J. S. Lian and Q. Jiang, *Chem. Phys. Lett.*, 2008, **455**, 202–206.
- Y. Hao, G. Meng, Z.-L. Wang, C. Ye and L. Zhang, *Nano Lett.*, 2006, **6**, 1650–1655.
- Y. Jiang, X.-M. Meng, J. Liu, Z.-Y. Xie, C.-S. Lee and S.-T. Lee, *Adv. Mater.*, 2003, **15**, 1195–1198.
- P. Prathap, N. Revathi, Y. P. V. Subbaiah, K. T. Ramakrishna Reddy and R. W. Miles, *Solid State Sci.*, 2009, **11**, 224–232.
- C. C. Klick and J. H. Schulman, *Solid State Phys.*, 1957, **5**, 97–172.
- B. Sotillo, P. Fernández and J. Piqueras, *J. Alloys Compd.*, 2013, **563**, 113–118.
- B. Alemán, P. Fernández and J. Piqueras, *J. Cryst. Growth*, 2010, **312**, 3117–3121.
- Y. Ortega, P. Fernández and J. Piqueras, *Nanotechnology*, 2007, **18**, 115606.
- X. Fang, Y. Bando, M. Liao, U. K. Gautam, C. Zhi, B. Dierre, B. Liu, T. Zhai, T. Sekiguchi, Y. Koide and D. Golberg, *Adv. Mater.*, 2009, **21**, 2034–2039.
- Z.-G. Chen, J. Zou, G. Liu, H. F. Lu, F. Li, G. Lu and H. M. Cheng, *Nanotechnology*, 2008, **19**, 055710.
- Y. G. Liu, P. Feng, X. Y. Xue, S. L. Shi, X. Q. Fu, C. Wang, Y.-G. Wang and T.-H. Wang, *Appl. Phys. Lett.*, 2009, **90**, 042109.
- J. Zhang, Y. Wang, J. Zhang, Z. Lin, F. Huang and J. Yu, *ACS Appl. Mater. Interfaces*, 2013, **5**, 1031–1037.
- M. Hafeez, T. Zhai, A. S. Bhatti, Y. Bando and D. Golberg, *J. Phys. Chem. C*, 2012, **116**, 8297–8304.
- D. Barreca, E. Tondello, D. Lydon, T. R. Spalding and M. Fabrizio, *Chem. Vap. Deposition*, 2003, **9**, 93.
- D. Barreca, A. Gasparotto, C. Maragno, E. Tondello and C. Sada, *Chem. Vap. Deposition*, 2004, **10**, 229.
- Q. Li and C. Wang, *Appl. Phys. Lett.*, 2003, **83**, 359–361.
- D. Barreca, A. Gasparotto, C. Maragno and E. Tondello, *J. Electrochem. Soc.*, 2004, **151**, G428.
- B. Sotillo, P. Fernández and J. Piqueras, *J. Cryst. Growth*, 2012, **348**, 85–90.
- Y. Ortega, P. Fernández and J. Piqueras, *J. Appl. Phys.*, 2009, **105**, 054315.
- Y. Ortega, D. Häussler, J. Piqueras, P. Fernández and W. Jäger, *Phys. Status Solidi A*, 2012, **209**, 1487–1492.
- J. G. Wen, J. Y. Lao, D. Z. Wang, T. M. Kyaw, Y. L. Foo and Z. F. Ren, *Chem. Phys. Lett.*, 2003, **372**, 717–722.
- Z. L. Wang, *J. Phys.: Condens. Matter*, 2004, **16**, R829–R858.
- D. Moore and Z. L. Wang, *J. Mater. Chem.*, 2006, **16**, 3898–3905.
- D. Moore, C. Ronning, C. Ma and Z. L. Wang, *Chem. Phys. Lett.*, 2004, **385**, 8–11.
- M.-Y. Lu, M.-P. Lu, Y.-A. Cung, M.-J. Chen, Z. L. Wang and L.-J. Chen, *J. Phys. Chem. C*, 2009, **113**, 12878–12882.
- H. Koelmans, *J. Phys. Chem. Solids*, 1960, **17**, 69.

- 30 Y. Ortega, P. Fernández and J. Piqueras, *J. Nanosci. Nanotechnol.*, 2010, **10**, 502.
- 31 Z. Wang, L. L. Daemen, Y. Zhao, C. S. Zha, R. T. Downs, X. Wang, Z. L. Wang and R. J. Hemley, *Nat. Mater.*, 2005, **4**, 922–927.
- 32 J. Li, Q. Zhang, L. An, L. Qin and J. Liu, *J. Solid State Chem.*, 2008, **181**, 3116–3120.
- 33 D. Moore, Y. Ding and Z. L. Wang, *Angew. Chem., Int. Ed.*, 2006, **45**, 5150–5154.
- 34 Y.-C. Zhu, Y. Bando and L.-W. Yin, *Adv. Mater.*, 2004, **16**, 331–334.
- 35 A. Béré and A. Serra, *Phys. Rev. B: Condens. Matter*, 2003, **68**, 033305.
- 36 J. F. Scott, T. C. Damen, W. T. Silfvast, R. C. C. Leite and L. E. Cheesman, *Opt. Commun.*, 1970, **1**, 397–399.
- 37 H. M. Fan, X. F. Fan, Z. H. Ni, Z. X. Shen, Y. P. Feng and B. S. Zou, *J. Phys. Chem. C*, 2008, **112**, 1865–1870.